

A comprehensive micro-scale model for transport and reaction in intermediate temperature solid oxide fuel cells

Jin Hyun Nam*, Dong Hyup Jeon

School of Mechanical and Aerospace Engineering, Seoul National University, San 56-1, Shilim-dong, Gwanak-gu, Seoul 151-744, Republic of Korea

Received 8 August 2005; received in revised form 21 September 2005; accepted 29 September 2005

Available online 23 November 2005

Abstract

A comprehensive model for detailed description of micro-scale transport and electro-chemical reaction in intermediate temperature SOFCs (solid oxide fuel cells) was developed by combining many relevant theoretical and experimental researches. Dependence of electro-chemical performance of PEN (positive electrode/electrolyte/negative electrode) on micro-structural parameters of electrodes was investigated through numerical simulation. Spatial distribution of transfer current density confirmed that TPBs (three phase boundaries) at electrode/electrolyte interface were most active for electro-chemical reaction and its contribution to overall reaction increased at higher current densities. Spatial gradient of total pressure in cathode was found to facilitate oxygen transport while that in anode hinder hydrogen transport. Among various micro-structural parameters for electrodes, particle diameter was found to be the most important one that governs the PEN performance; smaller particle diameter decreased activation overpotential with larger TPB length, while increasing mass transport resistance and concentration overpotential with smaller pore diameter. The proposed micro-model was found successful in micro-structural characterization of PEN performance, and thus believed to serve as a bridge connecting micro-scale models and macro-scale calculations.

© 2005 Published by Elsevier Ltd.

Keywords: Fuel cell; SOFC (solid oxide fuel cell); PEN (positive electrode/electrolyte/negative electrode); Micro-scale model; TPB (three phase boundary)

1. Introduction

SOFC (solid oxide fuel cell) is an energy conversion device that directly converts chemical energy of gaseous fuel to electricity [1,2]. Electro-chemical reaction in SOFC is completed in PEN (positive electrode/electrolyte/negative electrode); oxygen reduction reaction occurs in the cathode, detached oxygen ions migrate from cathode to anode through the electrolyte, and hydrogen oxidation reaction occurs in the anode. Typically, PENs are made of a solid electrolyte made of YSZ (yttria-stabilized zirconia), a cermet anode made of Ni/YSZ (nickel and YSZ), and a composite cathode made of LSM/YSZ (strontium-doped lanthanum manganite and YSZ).

The output potential of SOFC φ^{FC} may be expressed as

$$\varphi^{FC} = \varphi^o - \Delta\varphi^{PEN} - \Delta\varphi^{BP} - \Delta\varphi^{FF}, \quad (1)$$

where φ^o is the Nernst potential or OCP (open circuit potential)

$$\varphi^o = -\frac{\Delta g_f^o}{2F} + \frac{R_g T}{2F} \ln \left(\frac{p_{H_2, \infty}}{p_{H_2O, \infty}} \left(\frac{p_{O_2, \infty}}{100,000} \right)^{1/2} \right) \quad (2)$$

(pressures are in Pa)

and $\Delta\varphi^{PEN}$, $\Delta\varphi^{BP}$ and $\Delta\varphi^{FF}$ denote the potential loss in PEN, the potential loss due to bipolar plates, and that due to flow field effects, respectively. Main part of $\Delta\varphi^{BP}$ is contact resistance and non-uniform current generation due to interconnect rib geometry. Variation of channel conditions along the flow direction comprises $\Delta\varphi^{FF}$ ($\Delta\varphi^{BP}$ and $\Delta\varphi^{FF}$ were not considered in this study). Note that the present model is not limited to planar geometries and can be implemented in radial coordinates to represent tubular SOFCs. The potential loss in PEN $\Delta\varphi^{PEN}$ can be decomposed as

$$\begin{aligned} \Delta\varphi^{PEN} &= \Delta\varphi_E + \Delta\varphi_A + \Delta\varphi_C \\ &= (\Delta\varphi_{ohm})_E + (\Delta\varphi_{ohm} + \Delta\varphi_{act} + \Delta\varphi_{conc})_A \\ &\quad + (\Delta\varphi_{ohm} + \Delta\varphi_{act} + \Delta\varphi_{conc})_C \end{aligned} \quad (3)$$

* Corresponding author. Tel.: +82 2 880 1656; fax: +82 2 883 0179.
E-mail addresses: akko2@snu.ac.kr (J.H. Nam), dhjeon1@snu.ac.kr (D.H. Jeon).

Here $\Delta\varphi_{\text{ohm}}$ are ohmic losses due to ionic and electronic resistances of the electrolyte and electrodes, $\Delta\varphi_{\text{act}}$ are activation losses due to irreversibility of electro-chemical reaction at TPBs (three phase boundaries), and $\Delta\varphi_{\text{conc}}$ are concentration losses due to mass transport resistance in the electrodes. Because of complicated interaction between those losses, it is rather difficult to determine what fraction of anodic or cathodic loss is due to ohmic, activation or concentration polarizations.

High performance of SOFC largely relies on the optimal transport and the electro-chemical reaction in porous electrodes, which in turn requires the optimal design of micro-structures of porous electrodes. Detailed micro-scale models for transport and reaction in SOFC is indispensable to understand the phenomena, and to predict and enhance its electro-chemical performance.

Micro-structures of porous electrodes are generally modeled as random packing systems made of electronic particles for transport of electrons, ionic particles for transport of ions, and interstitial pores for transport of gas species, as shown in Fig. 1a. The porosity ε , the volume fraction of electronic phase ϕ_{el} , and the diameters d_{el} , d_{io} of the electronic and ionic particles affect the effective electronic and ionic conductivities (ohmic loss), the effective TPB length (activation loss), and the effective mass transport properties (concentration loss) through the percolation for the continuity of each electronic, ionic and gas phase. Listed below are the related previous researches, adopted in this study.

- Monte-Carlo resistor network simulations for SOFCs based on lattice or random packing of binary spherical particles [3–7];
- Studies on statistical properties of random packing of binary spherical particles [8–10];
- Continuum micro-scale models for SOFCs based on the statistical properties [11–16];
- Experimental observations on anodic activation overpotential for Ni/YSZ cermet anodes [17–23] and cathodic activation overpotential for LSM/YSZ composite cathodes [24–29];
- Dusty-gas model for parallel flow and diffusion through porous media [30–32].

In Monte-Carlo simulations by Sunde [3–5] and others [6,7], individual particle location and connection to other particles were stored and used to construct resistor networks, followed by calculation of electrical potential at each particle location. In spite of its advantages in predicting the percolation behaviors of binary particle systems, the use of resistor network models were limited to problems with small specimen size due to high computational costs, primarily to estimate macro-scale properties of porous electrodes.

In continuum micro-scale models [11–16], the effective properties of porous electrodes were estimated based on the statistical properties of random packing systems of binary spherical

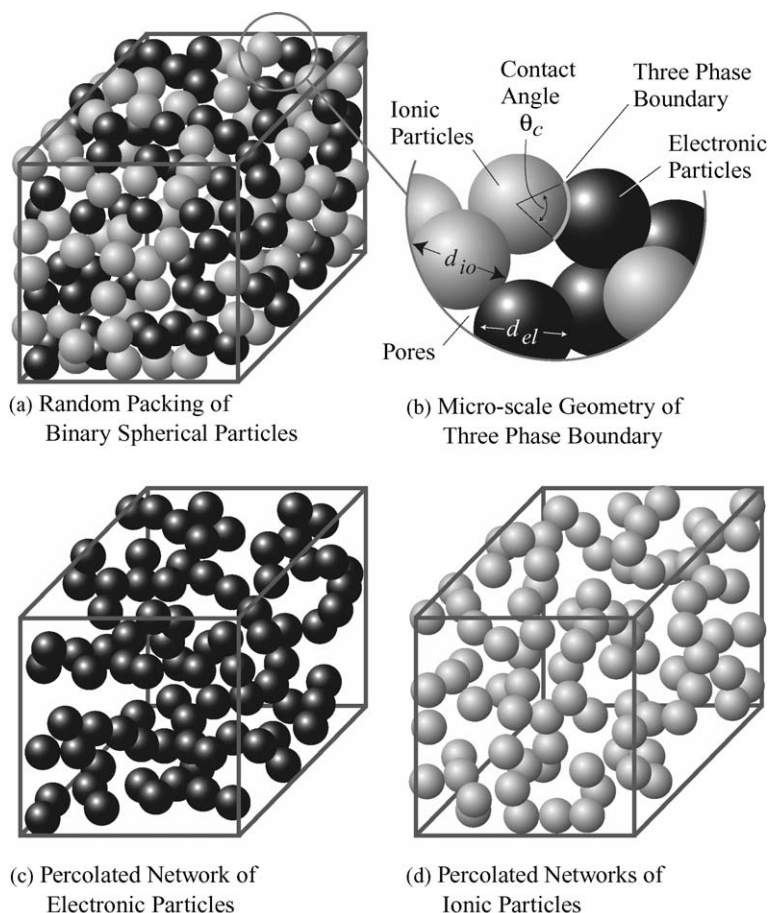


Fig. 1. Micro-structural modeling of a porous electrode as a random packing system of binary spherical particles.

particles [8–10]. This approach enables detailed macro-scale prediction of electro-chemical processes in porous electrodes, while allowing preservation of important micro-structural properties of porous electrodes (percolation behavior and coordination number). So far, however, these continuum micro-scale models were used to predict the electro-chemical characteristics of one electrode only, anode or cathode, not whole PEN.

We tried to make the present micro-scale model accurate in micro-scale description of the electro-chemical processes, as well as practical in macro-scale prediction of the performance of PEN or SOFC. The effective properties were derived from the micro-structural parameters of porous electrodes. Experiments on electro-chemical reaction kinetics with well-defined TPB length [23,29] were used to model the behaviors of activation overpotential at TPBs. Gas phase transport was calculated by the dusty-gas model [30–32], which considers binary diffusion, Knudsen diffusion, and Darcy flow in the porous electrodes.

2. Micro-scale sub-models

2.1. Electro-chemical properties of electrodes

In random packing systems of binary spherical particles, there exists a local continuous path in each kind of particles as shown in Fig. 1c and d. These particle clusters are called as percolated when they form globally continuous paths for their own particles. The probability to form percolated cluster or to complete percolation is statistically determined as a function of particle size, and volume fraction of each phase, etc.

Studies on statistical properties of the random packing systems of binary spherical particles have been conducted by several researchers [8–10], which leads to theory of coordination number (number of contacts with other particles). The percolation behavior of random packing systems of binary spherical particles was found well described by the coordination number theory, using the threshold coordination number for completion of percolation.

The statistical properties were used in continuum micro-scale models [11–16] to estimate the effective electronic and ionic conductivities, which show strong percolation behavior, and also the effective TPB length. Although real micro-structures of composite electrodes are different from the random packing systems, such approaches have been proven successful in correlating micro-structural parameters and electro-chemical performance of porous electrodes.

Average total coordination number for electronic particles is [9]:

$$Z_{el} = 3 + \frac{Z - 3}{n_{el} + (1 - n_{el})\alpha^2}, \quad (4)$$

and that for ionic particles is

$$Z_{io} = 3 + \frac{(Z - 3)\alpha^2}{n_{el} + (1 - n_{el})\alpha^2}, \quad (5)$$

where α is the size ratio of ionic particles to electronic particles ($\alpha \equiv d_{io}/d_{el}$), Z is the average coordination number for random

packing systems of spherical particles, which is 6, and n_{el} is number fraction of electronic particles. The number fraction is related with volume fraction of electronic phase ϕ_{el} as ($n_{io} = 1 - n_{el}$)

$$n_{el} = \frac{\alpha^3 \phi_{el}}{1 - \phi_{el} + \alpha^3 \phi_{el}}. \quad (6)$$

The coordination number between i -phase particle and j -phase particle is Z_{i-j} , given as

$$Z_{i-j} = n_j \frac{Z_i Z_j}{Z}. \quad (7)$$

The probability of an i -phase particle to belong to the percolated clusters of the same phase is given by P_i [8]:

$$P_i = \left[1 - \left(\frac{4.236 - Z_{i-i}}{2.472} \right)^{2.5} \right]^{0.4}, \quad (8)$$

which results in zero probability at the percolation threshold.

The effective conductivity of i -phase in a porous electrode can be determined from the porosity ε , volume fraction ϕ_i , and percolation probability P_i for i -phase as

$$\sigma_i = \sigma_i^0 [(1 - \varepsilon)\phi_i P_i]^m, \quad (9)$$

where σ_i^0 is the conductivity for solid i -phase material. The electrical conductivities of nickel, LSM and YSZ are presented in Table 1, referring to several studies [33–35].

The exponent m in Eq. (9) depends on the distribution of the i -phase material in space, e.g., $m = 1$ is correspondent to

Table 1

Properties and operation conditions for micro-scale calculation of PEN performance

Properties and conditions	Value or expression
T	700 °C
ϕ^{FC}	0.7 V
ϕ^o	$\frac{247340 - 54.85T}{2F} + \frac{R_g T}{2F} \left(\frac{p_{H_2}}{p_{H_2O}} \left(\frac{p_{O_2}}{100,000} \right)^{1/2} \right) \text{ V [2]}$
$(p_i)_A, (p_i)_C$	1 atm
$x_{H_2, \infty}$ or $1 - x_{H_2O, \infty}$	0.21
$x_{O_2, \infty}$ or $1 - x_{N_2, \infty}$	0.70
L_A, L_C	50 μm
L_E	10 μm
σ_{YSZ}^o	$3.34 \times 10^4 \exp \left(-\frac{10300}{T} \right) \text{ S/m [33]}$
σ_{Ni}^o	$3.27 \times 10^6 - 1065.37 \text{ S/m [34]}$
σ_{LSM}^o	$\frac{8.855 \times 10^7}{T} \exp \left(\frac{1082.5}{T} \right) \text{ S/m [35]}$
$D_{H_2-H_2O}$	$4.28 \times 10^{-4} \frac{T^{1.75}}{p_t} \text{ m}^2/\text{s [42,43]}$
$D_{O_2-N_2}$	$9.75 \times 10^{-5} \frac{T^{1.75}}{p_t} \text{ m}^2/\text{s [42,43]}$
$\varepsilon_A, \varepsilon_C$	0.3
τ_A, τ_C	3.0 [44]
$(\phi_{el})_A, (\phi_{el})_C$	0.5
$(d_{el})_A, (d_{io})_A, (d_{el})_C, (d_{io})_C$	1 μm
θ_c	30° [11–16]

fully percolated *i*-phase material to form straight conduction path with uniform cross-sectional area (upper bound of conductivity). Due to the tortuosity of percolated particle network and repeated constriction at the necks of particle contacts as shown in Fig. 1, the exponent *m* is generally larger than one. In the present model, *m* = 1.5 was adopted from the Bruggeman EMT (effective medium theory). However, Eq. (9) seems to slightly over-estimate the effective conductivities, considering that observed effective electronic conductivities of Ni/YSZ cermet were about 1000 S/cm for ϕ_{el} around 0.45 at 800 °C [34,36].

TPB length is one of the most important micro-structural parameters that govern the electro-chemical performance of porous electrodes. Larger TPB length means more reaction sites, and thus lower activation loss in the electrodes. In random packing systems, TPBs are formed by the contacts of percolated electronic particles and percolated ionic particles and thus depends on Z_{io-el} in Eq. (7). In Fig. 1b, the neck diameter d_c was assumed dependent on the smaller particle diameter and the contact angle θ_c as

$$d_c = \sin\left(\frac{\theta_c}{2}\right) \min(d_{io}, d_{el}), \quad (10)$$

where θ_c of 30° ($d_c \approx 0.26d_{el}$ for $d_{el} = d_{io}$) was generally assumed [11–16]. In fact, θ_c is not a purely geometric parameter for particle contacts, though presented as such in Fig. 1b, due to the particle size distribution and the existence of unsuccessful TPB contacts. Thus, θ_c may be understood as a changeable constant to properly estimate TPB length in electrodes.

Then, the volume specific TPB length l_{tpb}^V (m/m³) is determined as

$$l_{tpb}^V = \pi d_c N_t n_{io} n_{el} \frac{Z_{io} Z_{el}}{Z} P_{io} P_{el}, \quad (11)$$

where N_t (#/m³) is the number density of all particles, given as

$$N_t = \frac{1 - \varepsilon}{(\pi/6)d_{el}^3 (n_{el} + (1 - n_{el})\alpha^3)}. \quad (12)$$

When thickness of a porous electrode is small, TPB length formed by direct contacts of percolated electronic particles with the surface of a solid electrolyte becomes important. The electro-chemical efficiency of the TPBs with respect to the distance from the electrolyte surface has been discussed by the authors [7]. The area specific TPB length l_{tpb}^A (m/m²) at the electrolyte surface is determined by the number of percolated electronic particles contained in the thickness of d_{el} as

$$l_{tpb}^A = \pi d_{el} \sin\left(\frac{\theta_c}{2}\right) N_t d_{el} n_{el} P_{el}. \quad (13)$$

2.2. Electro-chemical reaction kinetics at TPBs

The electro-chemical reaction in porous electrodes mainly occurs at TPBs where electronic phase for conduction of electrons, ionic phase for migration of ions, and pores for transport of gas molecules co-exist. This has been substantiated by the inverse proportionality of activation overpotential with

respect to TPB length, observed in several experimental studies using Ni/YSZ anodes [17,21–23] and LSM/YSZ cathodes [24,25,27,29] with well-defined TPB lengths. Then, a correlation (or a reaction kinetics) between TPB length specific transfer current density i_{tpb} (A/m) and activation overpotential $\Delta\varphi_{act}$ for TPBs of Ni/YSZ interface, and that for TPBs of LSM/YSZ interface, can be obtained.

The correlation for H₂ oxidation reaction at TPBs of Ni/YSZ interface was derived from the behavior of the activation overpotential of pattern Ni anode on YSZ substrate measured by Bieberle et al. [23] as

$$\begin{aligned} (i_{tpb})_A &= f_A(T, p_{H_2}, p_{H_2O}, \Delta\varphi_{act}) \\ &= \frac{\Delta\varphi_{act}}{1.645 p_{H_2}^{-0.11} p_{H_2O}^{-0.67} \exp(10,212/T) \times 10^{-4\Delta\varphi_{act}}}, \end{aligned} \quad (14a)$$

where the ranges of the experimental conditions were 673–973 K for *T*, 10⁴ to 8.8 × 10⁴ Pa for *p*_{H₂}, 40–2000 Pa for *p*_{H₂O}, and 0–300 mV for $\Delta\varphi_{act}$.

Jiang and Ramprakash [19,20] also suggested an empirical correlation similar to the Butler–Volmer equation for a cermet anode at higher temperatures (850 °C < *T* < 1000 °C). The reaction orders with respect to *p*_{H₂} and *p*_{H₂O}, and the activation energy *E_a* were observed about 0.1 and 0.5, and 70 kJ/mol, respectively [19,20], which are well matched with 0.11 and 0.67, and 85 kJ/mol in Eq. (14a). Abrupt transition in the reaction order for *p*_{H₂O} at about 14,000 Pa was also observed during changing *p*_{H₂O} from 4000 to 20,000 Pa [19,20], which indicates that catalytic effect of water vapor reaches maximum at that pressure level. Therefore, Eq. (14a) was used for *p*_{H₂O} lower than 14,000 Pa, and the following Eq. (14b) was used for *p*_{H₂O} higher than 14,000 Pa:

$$\begin{aligned} (i_{tpb})_A &= f_A(T, p_{H_2}, p_{H_2O}, \Delta\varphi_{act}) \\ &= \frac{\Delta\varphi_{act}}{1.645 p_{H_2}^{-0.11} 14,000^{-0.67} \exp(10,212/T) \times 10^{-4\Delta\varphi_{act}}}. \end{aligned} \quad (14b)$$

Similarly, the rate equation for O₂ reduction reaction at TPBs of LSM/YSZ interface was derived from the behavior of the activation overpotential of pattern LSM cathode on YSZ substrate measured by Radhakrishnan et al. [29] as

$$\begin{aligned} (i_{tpb})_C &= f_C(T, p_{O_2}, \Delta\varphi_{act}) \\ &= \frac{R_g T}{4F} \frac{2 \sinh(2F\Delta\varphi_{act}/R_g T)}{0.00136 p_{O_2}^{-0.25} \exp(17,401/T)}, \end{aligned} \quad (15)$$

where the ranges of the experimental conditions were 650–800 °C for *T*, and 1000–100,000 Pa for *p*_{O₂}. In Eq. (15), the exchange current density was calculated from the slopes of charge transfer resistance with respect to TPB length, tabulated in Radhakrishnan et al. (their Table 1) [29]. And the standard Butler–Volmer equation was used to model the non-linear behavior of the transfer current/activation overpotential curve. The measured *E_a* of 1.5 eV [26,29] was used to model the dependence of the exchange current density on temperature.

2.3. Mass transport properties of electrodes

Viscous flow and diffusion occur simultaneously during the mass transport of binary gases through porous electrodes. For evaluation of the total molar flux, the dusty-gas model [30–32] was adopted because it was reported more accurate than Fick's or Maxwell–Stefan model [37–39]. From parallel summation of fluxes due to diffusion and viscous flow, total molar flux \mathbf{n}_i of species i becomes

$$\mathbf{n}_i = \mathbf{n}_i^f + \mathbf{n}_i^d. \quad (16)$$

Here \mathbf{n}_i^f and \mathbf{n}_i^d denote the molar fluxes due to viscous flow and diffusion, respectively. The molar flux due to viscous flow through porous electrodes is described by Darcy law as [40]:

$$\mathbf{n}_i^f = c_i \mathbf{u} = \frac{p_i}{R_g T} \frac{K}{\mu} \nabla p_t, \quad (17)$$

where p_t is the total pressure, p_i the partial pressure of species i , and K is the flow permeability which depends on micro-structure of the porous electrodes. For random packing systems of spherical particles, Carman–Kozeny correlation is generally used to evaluate the flow permeability.

Firstly, the hydraulic diameter is calculated as

$$d_h = \frac{4}{A_0} \frac{\varepsilon}{1 - \varepsilon}, \quad (18)$$

where A_0 is the specific surface area based on the solid volume. For random packings of binary electronic and ionic particles with the size ratio α (bi-modal size distribution), A_0 is given as

$$A_0 = \frac{6}{d_{el}} \frac{n_{el} + (1 - n_{el})\alpha^2}{n_{el} + (1 - n_{el})\alpha^3}, \quad (19)$$

where above Eq. (19) reduces to $A_0 = 6/d_{el}$ when $\alpha = 1$.

Carman–Kozeny correlation determines flow permeability as

$$K = \frac{\varepsilon^3}{k_K (1 - \varepsilon)^2 A_0^2}, \quad (20)$$

where the Kozeny constant k_K is around 5 for porous media made of spherical particles.

The molar flux due to diffusion \mathbf{n}_i^d can be determined by solving the Maxwell–Stefan equation including the effect of Knudsen diffusion as

$$\frac{1}{R_g T} \nabla p_i = \sum_{j=1}^n \frac{x_i \mathbf{n}_j^d - x_j \mathbf{n}_i^d}{D_{ij}^\varepsilon} - \frac{\mathbf{n}_i^d}{D_{iK}^\varepsilon}. \quad (21)$$

Here D_{ij} is the binary diffusivity for the pair of species i and j , D_{iK} the Knudsen diffusivity for species i , and the superscript ε denotes that these diffusivities are the effective properties in the porous media.

The binary diffusivities for $\text{H}_2/\text{H}_2\text{O}$ in anodes and O_2/N_2 in cathodes may be determined using the kinetic theory [41]. In this study, however, the correlation due to Fuller et al. [43] was used to determine the binary diffusivities at high temperature, according to the recommendation of Todd and Young [42] in their review article on thermodynamic properties of fuel cell

gases. The binary diffusivity for the pair of species i and j can be determined from

$$D_{ij} = \frac{0.00143 T^{1.75}}{p_t M_{ij}^{1/2} (V_i^{1/3} + V_j^{1/3})}, \quad (22)$$

where p_t is the pressure (bar), M_{ij} is the mean molecular mass (kg/kmol)

$$M_{ij} = 2 \left(\frac{1}{M_i} + \frac{1}{M_j} \right)^{-1}, \quad (23)$$

and V_i is the diffusion volume of species i (6.12 for H_2 , 13.1 for H_2O , 16.3 for O_2 , and 18.5 for N_2). Polynomial fitting functions for viscosities of fuel cell gases were also presented in Todd and Young [42], which were used for estimation of mixture viscosity in Eq. (17) after averaging based on mole fraction.

Solid structure in porous media reduces the diffusion rate as it limits the flow rate. In continuum region, the reduction of diffusivity due to the solid structure can be correlated with two micro-structural parameters, porosity and tortuosity. The effective binary diffusivity in porous media D_{ij}^ε is calculated as

$$D_{ij}^\varepsilon = \frac{\varepsilon}{\tau} D_{ij}, \quad (24)$$

where a correlation of $\varepsilon/\tau = \varepsilon^{1.5}$ may be used for general porous media according to the Bruggeman EMT. However, we assume that the tortuosity is about 3 and relatively constant for the porosity range of porous electrodes of SOFCs [44]. The above correlation assumes that pores are always percolated and the fraction of closed pore space is negligible.

When pore size becomes comparable to the mean free path of a gas molecule, the collision between gas molecules and solid structure act as an additional mass transport resistance [41]. The effective Knudsen diffusivity for species i is defined

$$D_{iK}^\varepsilon = \frac{\varepsilon}{\tau} D_{iK} = \frac{\varepsilon}{\tau} \frac{97}{2} d_p \sqrt{\frac{T}{M_i}}, \quad (25)$$

where M_i is the molecular mass (kg/kmol), and d_p is the mean pore diameter. In this calculation, the pore diameter is assumed similar to the hydraulic diameter ($d_p \approx d_h$).

3. Governing equations

3.1. Conservation of electrical currents

Conservation of electronic current in a finite volume i is stated as (Fig. 2)

$$\sum_{j=e,w,n,s,t,b} I_{el,i \rightarrow j} = I_{tpb,j}, \quad (26)$$

where $I_{el,i \rightarrow j}$ (A) denotes an electronic current from a finite volume i to a neighboring finite volume j through a common area A_{ij} (m^2), and $I_{tpb,i}$ (A) denotes a transfer current from ionic phase to electronic phase in the finite volume i (an electronic current source due to electro-chemical reaction at TPBs). In ordinary operation of SOFCs, $I_{tpb,i}$ is negative in anodes

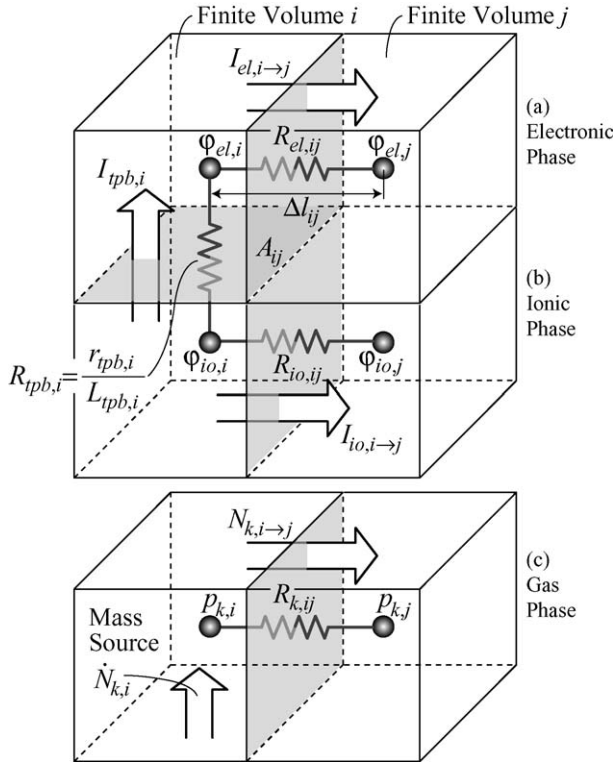


Fig. 2. Conservation of electrical (electronic and ionic) currents and gas species in finite volumes.

as current flows from electronic to ionic phase, and positive in cathodes as current flows from ionic phase to electronic phase.

Then, Eq. (26) can be rewritten in terms of electronic resistance between two finite volumes $R_{el,ij}$ (Ω) as

$$\sum_j \frac{\varphi_{el,i} - \varphi_{el,j}}{R_{el,ij}} = I_{tpb,i}, \quad (27)$$

where $R_{el,ij} = \Delta l_{ij} / \sigma_{el} A_{ij}$.

Similarly, conservation of ionic current in a finite volume i is stated as

$$\sum_j I_{io,i \rightarrow j} = -I_{tpb,i}. \quad (28)$$

At this time, $I_{tpb,i}$ is expressed in terms of charge transfer resistance in the finite volume i $R_{tpb,i}$ (Ω) as $I_{tpb,i} = \Delta \varphi_{act,i} / R_{tpb,i}$, where $R_{tpb,i}$ is determined from $R_{tpb,i} = r_{tpb,i} / L_{tpb,i}$. Here $L_{tpb,i}$ (m) denotes TPB length contained in the finite volume i and calculated as $L_{tpb,i} = l_{tpb}^V \Delta V_i$ or $L_{tpb,i} = l_{tpb}^A \Delta A_i$.

Then, Eq. (28) can be rewritten in terms of ionic resistance between two finite volumes $R_{io,ij}$ (Ω) as

$$\sum_j \frac{\varphi_{io,i} - \varphi_{io,j}}{R_{io,ij}} = -\frac{\Delta \varphi_{act,i}}{R_{tpb,i}}, \quad (29)$$

where $R_{io,ij} = \Delta l_{ij} / \sigma_{io} A_{ij}$.

During iterative calculation, $r_{tpb,i}$ is determined based on the calculated $i_{tpb,i}$, not on calculated $\Delta \varphi_{act,i}$, as

$$(r_{tpb,i})_A = \frac{\Delta \varphi_{act,i}}{i_{tpb,i}} = \frac{f_A^{-1}(T, p_{H_2}, p_{H_2O}, i_{tpb})}{i_{tpb,i}}, \quad (30)$$

$$(r_{tpb,i})_C = \frac{\Delta \varphi_{act,i}}{i_{tpb,i}} = \frac{f_C^{-1}(T, p_{O_2}, i_{tpb})}{i_{tpb,i}}, \quad (31)$$

where this procedure was found to enhance the stability of solution when sufficient under-relaxation in the transfer current density calculation is used.

The Nernst potential φ^0 and the target cell potential φ^{FC} were applied as a boundary condition at the anode-side of PEN and that at the cathode-side of PEN. Then, electronic potential is higher than ionic potential in anodes, and lower than ionic potential in cathodes. Local activation overpotential $\Delta \varphi_{act,i}$ is calculated as the difference between higher potential and lower potential, subtracted by concentration overpotential, as

$$\begin{aligned} (\Delta \varphi_{act,i})_A &= (\varphi_{el,i} - \varphi_{io,i}) - \Delta \varphi_{conc,i} \\ &= (\varphi_{el,i} - \varphi_{io,i}) + \frac{R_g T}{2F} \ln \left(\frac{p_{H_2,i} p_{H_2O,\infty}}{p_{H_2,\infty} p_{H_2O,i}} \right), \end{aligned} \quad (32)$$

$$\begin{aligned} (\Delta \varphi_{act,i})_C &= (\varphi_{io,i} - \varphi_{el,i}) - \Delta \varphi_{conc,i} \\ &= (\varphi_{io,i} - \varphi_{el,i}) + \frac{R_g T}{4F} \ln \left(\frac{p_{O_2,i}}{p_{O_2,\infty}} \right). \end{aligned} \quad (33)$$

3.2. Mass conservation of gas species

The transport of fuel and oxidant in porous electrodes alters the distribution of local current density and the performance of PEN through concentration overpotential. Thus, careful consideration on the mass transport is important, especially at higher current density operation.

Conservation of gas species k in a finite volume i in porous electrode is stated as

$$\sum_j N_{k,i \rightarrow j} = \dot{N}_{k,i}, \quad (34)$$

where $N_{k,i \rightarrow j}$ is molar flow (mol/s) of species k through the common area of a finite volume i to a neighboring finite volume j , and $\dot{N}_{k,i}$ (mol/s) is a mass source in the finite volume i due to electro-chemical reaction at TPBs.

From the definition of $I_{tpb,i}$, $\dot{N}_{H_2,i}$ is $I_{tpb,i} / 2F$ for hydrogen, $\dot{N}_{H_2O,i}$ is $-I_{tpb,i} / 2F$ for water vapor, $\dot{N}_{O_2,i}$ is $-I_{tpb,i} / 4F$ for oxygen, and $\dot{N}_{N_2,i}$ is zero for nitrogen. The positive sign indicates that direction of mass transport is the same as that of current.

In case of binary gas transport of H_2/H_2O in anodes, and O_2/N_2 in cathodes, molar flux equations can be explicitly given. The Maxwell–Stefan equation of Eq. (21) is expanded for binary

species 1 and 2 as

$$\begin{pmatrix} -\frac{x_2}{D_{12}^e} - \frac{1}{D_{1K}^e} & \frac{x_1}{D_{12}^e} \\ \frac{x_2}{D_{12}^e} & -\frac{x_1}{D_{12}^e} - \frac{1}{D_{2K}^e} \end{pmatrix} \begin{pmatrix} n_1^d \\ n_2^d \end{pmatrix} = \frac{1}{R_g T} \begin{pmatrix} \nabla p_1 \\ \nabla p_2 \end{pmatrix}, \quad (35)$$

using the relation of $x_i = p_i/p_t$.

Matrix inversion of Eq. (35) results in diffusive flux equations. By adding the molar flux due to Darcy flow shown in Eq. (17), the total molar flux equations for species 1 and 2 can be given as

$$\begin{aligned} \mathbf{n}_1 &= -\frac{1}{R_g T} (k_1 \nabla p_1 + k_2 p_1 \nabla p_t), \\ \mathbf{n}_2 &= -\frac{1}{R_g T} (k_3 \nabla p_2 + k_4 p_2 \nabla p_t). \end{aligned} \quad (36)$$

From molar mass fluxes in Eq. (36), $N_{1,i \rightarrow j}$ and $N_{2,i \rightarrow j}$ can be discretized as

$$\begin{aligned} N_{1,i \rightarrow j} &= \frac{A_{ij}}{R_g T} \left[(k_1 + k_2 p_1) \frac{p_{1,i} - p_{1,j}}{\Delta l_{ij}} + k_2 p_1 \frac{p_{2,i} - p_{2,j}}{\Delta l_{ij}} \right], \\ N_{2,i \rightarrow j} &= \frac{A_{ij}}{R_g T} \left[(k_3 + k_4 p_2) \frac{p_{2,i} - p_{2,j}}{\Delta l_{ij}} + k_4 p_2 \frac{p_{1,i} - p_{1,j}}{\Delta l_{ij}} \right], \end{aligned} \quad (37)$$

where the mass transport coefficients are given as

$$\begin{aligned} k_1 &= \frac{D_{12}^e D_{1K}^e}{D_{12}^e + D_{mK}^e}, \quad k_3 = \frac{D_{12}^e D_{2K}^e}{D_{12}^e + D_{mK}^e}, \\ k_2 &= k_4 = \frac{1}{p_t} \frac{D_{1K}^e D_{2K}^e}{D_{12}^e + D_{mK}^e} + \frac{K}{\mu}, \end{aligned} \quad (38)$$

with the mixture Knudsen diffusivity, defined as $D_{mK}^e = x_1 D_{2K}^e + x_2 D_{1K}^e$.

Partial pressures of H_2 and H_2O at the anode-side boundary of PEN were the same as those in the anode channel by assuming negligible surface mass transfer resistance. Similarly, partial pressures of O_2 and N_2 at the cathode-side boundary of PEN were the same as those in the cathode channel. For n component gas transport ($n > 2$), the dusty-gas model becomes slightly more complicated as the coefficients for the mass flux equations should be numerically determined for each finite volume through inverse of n by n matrix.

3.3. Numerical procedures

Fig. 3 shows a one-dimensional domain of PEN for micro-scale calculation, discretized into finite volumes, along with electrical resistances. Also shown is a hydraulic analogy for the current transport in PEN; head h is correspondent to electrical potential ϕ ; flow resistances R_{ij} and R'_{ij} to electrical resistances $R_{el,ij}$, $R_{io,ij}$ and $R_{tpb,i}$; and flow rate Q to the electrical cur-

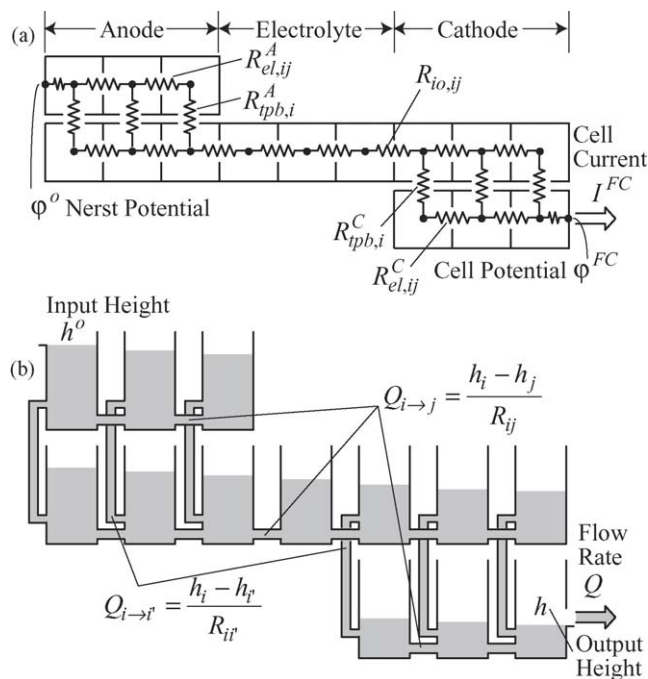


Fig. 3. An exemplary domain for micro-scale calculation of PEN performance, rendered with electrical resistances (a), and a hydraulic analogy for current conduction (b).

rent I . In general, the electrical resistance satisfy the relation $R_{el,ij} < R_{io,ij} \ll R_{tpb,i}$.

Overall numerical procedure is summarized as follows. Before starting the calculation, main variables are initialized: electronic potential in anode is the Nernst potential ϕ^0 , and that in cathode is the operating cell potential ϕ^{FC} ; ionic potential in anode, cathode and electrolyte is the average of the two as $(\phi^0 + \phi^{FC})/2$; gas composition in electrodes is the same as that in corresponding channels; transfer current density i_{tpb} is 0.

Potential calculation begins with the estimation of concentration overpotential based on Eqs. (32) and (33). Then, r_{tpb} is determined from Eqs. (30) and (31) for given i_{tpb} and ionic potential distribution is calculated by solving Eq. (29) using $r_{tpb} (\equiv r_{tpb,i}/L_{tpb,i})$. The obtained ionic potential distribution is used to determine i_{tpb} with considerable under-relaxation to ensure stable convergence. Then, electronic potential distribution is calculated by solving Eq. (27) using $I_{tpb} (\equiv i_{tpb} L_{tpb})$.

Concentration calculation starts by solving Eq. (34) with molar flux equations of Eq. (36) or (37) to obtain partial pressure distributions in electrodes. Finally, the convergence was monitored to ensure accuracy of solution (1.0×10^{-5} V for absolute potential, 0.1 Pa for absolute partial pressure, 1.0×10^{-5} for relative transfer current density).

4. Results and discussion

The electro-chemical performance of PEN was investigated, based on the properties and operation conditions, summarized in Table 1. The dependence of PEN performance on temperature was studied for three temperatures of 600, 700 and 800 °C (low temperature range of SOFC operation). Adopted models for the

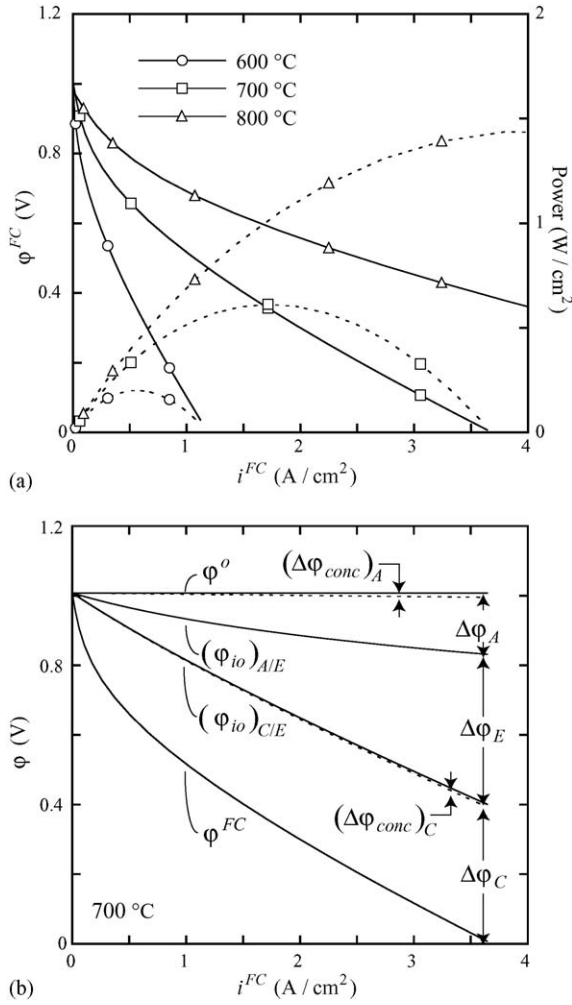


Fig. 4. Simulated PEN I - V performances at 600, 700 and 800 °C (a), and contribution of each component in PEN to overall potential loss at 700 °C (b).

electro-chemical reaction kinetics for H_2 oxidation at Ni/YSZ TPBs and O_2 reduction at LSM/YSZ TPBs are valid in that temperature range. Note that Bieberle et al. [23] conducted their experiments at temperatures between 400 and 700 °C, and Radhakrishnan et al. [29] at temperature between 650 and 800 °C.

The simulated performance of PEN, shown in Fig. 4a, matches the measured single-cell performance in Zhao and Virkar (their Fig. 5) [45], though simulated PEN geometry is not the same as theirs. Simulation predicted that the maximum power density is about 0.2 W/cm^2 for 600 °C, 0.6 W/cm^2 for 700 °C, and 1.4 W/cm^2 for 800 °C, and cell current density i^{FC} at operating cell potential of 0.7 V ($\Delta\phi^{PEN} \sim 0.3$ V) is about 0.13 A/cm^2 for 600 °C, 0.39 A/cm^2 for 700 °C, and 0.95 A/cm^2 for 800 °C. Although these figures are in fact impressive considering the low operation temperatures, SOFC using the same PEN may result in considerably lower performance due to contact resistances, non-uniform current generation due to interconnect rib geometry, and variation of fuel and oxidant concentration along the channel, as indicated by Eq. (1). The contribution of each component in PEN to overall potential loss at 700 °C is summarized in Fig. 4b.

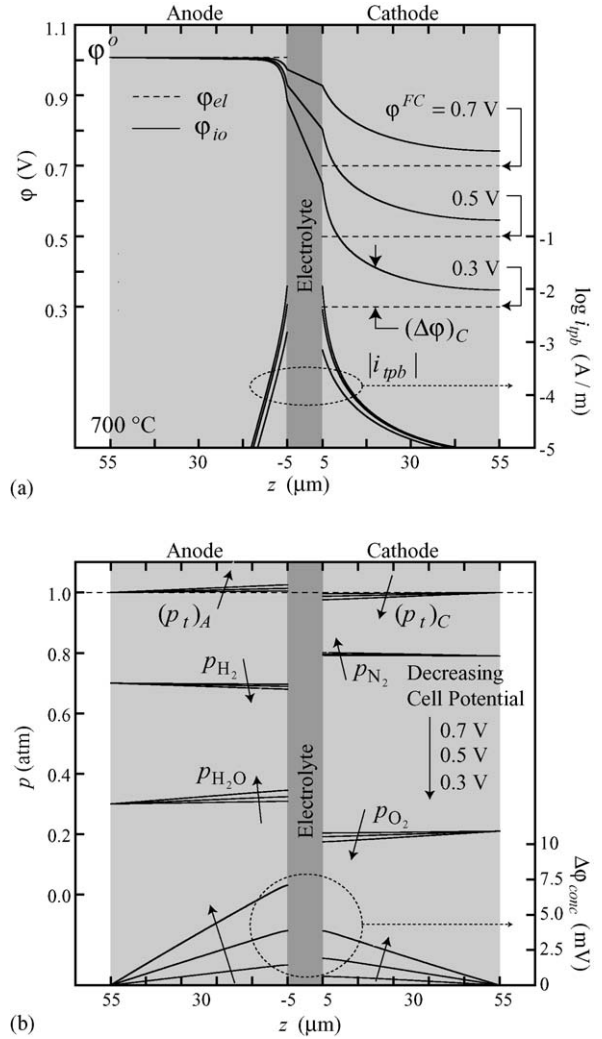


Fig. 5. Spatial distributions of electrical potentials and i_{tpb} in PEN (a), and those of concentrations and concentration activation overpotentials (b).

Spatial distribution of electrical potentials, current generation in PEN at 700 °C is shown in Fig. 5a. The electronic potential is presented higher than ionic potential in anode by adding the Nernst potential (Fig. 3). The potential loss in anode is observed relatively small at low current density in Fig. 5a, but it becomes slightly larger at high current density. However, the potential loss in cathode is always the largest among those in anode, cathode, and electrolyte, as also shown in Fig. 4b. Because current density of SOFC operation at low temperature (<800 °C) can hardly exceed 1 A/cm^2 in general, the cathodic potential loss is far more important than other losses.

Spatial distribution of i_{tpb} shown in Fig. 5a indicates that TPBs at the electrode/electrolyte interfaces are most active. Most of electro-chemical reaction in anode seems to occur within 10 μm distance from the electrolyte. However, the spatial gradient of ionic potential in cathode, which is proportional to the ionic current flowing through ionic particle network, implies considerable amount of electro-chemical reaction occurs at TPBs whose distance from the electrolyte is larger than 10 μm . It is also observed that i_{tpb} at a location always increases with

decrease in ϕ^{FC} (or increase in $\Delta\phi^{PEN}$), but its contribution to i^{FC} decreases when the location is far from the electrolyte.

Fig. 5b shows that concentration overpotentials are less than 10 mV, which indicates that the present PEN geometry with thin electrodes (50 μm anode and 50 μm cathode) is not limited by mass transport. It is interesting to observe that the total pressure in anode and that in cathode are not the same as those in corresponding channels (1 atm in anode and cathode channels). The total pressure in cathode is lower near the cathode/electrolyte interface due to consumption of oxygen molecules at TPBs. Then, the gradient in total pressure developed in cathode helps the transport of oxygen from channel towards the electrolyte.

Higher total pressure in anode near the anode/electrolyte interface is, however, not induced by the consumption of hydrogen at TPBs since exactly same amount of water vapor is produced simultaneously. Eq. (25) predicts that the Knudsen diffusivity of hydrogen is three times larger than that of water vapor. As pore size in anode becomes smaller, the difference in the effective diffusivities of hydrogen and water vapor gets larger due to the difference in Knudsen diffusivities of the two gases. Then, to transport the same amount of water vapor requires larger gradient in its concentration (or partial pressure) than to transport hydrogen does, which results in accumulation of water vapor near the anode/electrolyte interface. Note that the spatial gradient in total pressure developed in anode may act as an additional mass transport resistance for hydrogen.

The distributed electro-chemical reaction in anode, as shown in Fig. 5a, make it difficult to single out a representative activation overpotential $(\Delta\phi_{act})_A$ from anodic overpotential $\Delta\phi_A$. If we assume anodic concentration overpotential $(\Delta\phi_{conc})_A$ is well represented by its maximum at the anode/electrolyte interface as $(\Delta\phi_{conc})_A \equiv (\Delta\phi_{conc})_{A/E}$, the sum of ohmic and activation overpotential in anode can be determined as

$$(\Delta\phi_{ohm} + \Delta\phi_{act})_A = \Delta\phi_A - (\Delta\phi_{conc})_{A/E}, \quad (39)$$

and based on Eq. (39), area specific charge transfer resistance in anode $(r_p)_A$ is defined as

$$(r_p)_A = \frac{(\Delta\phi_{ohm} + \Delta\phi_{act})_A}{i^{FC}}. \quad (40)$$

Predicted $(r_p)_A$ in Fig. 6a exhibits somewhat weaker dependence on the sum of activation and ohmic overpotentials as $(r_p)_A \propto 10^{-2(\Delta\phi_{ohm} + \Delta\phi_{act})_A}$ than $r_{tpb,i}$ in anode, governed by Eq. (14) as $r_{tpb,i} \propto 10^{-4\Delta\phi_{act,i}}$. Similar trend is also observed in cathode in Fig. 6b. While Eq. (15) describes $i_{tpb,i} \sim \exp(2f\Delta\phi_{act,i})$ in cathode at high overpotential, the simulation leads to a relation $i^{FC} \sim \exp[1.1f(\Delta\phi_{ohm} + \Delta\phi_{act})_C]$, where $f = F/R_g T$. These reduced dependences on activation overpotentials in anode and cathode are believed to be related with the distributed electro-chemical reaction in the electrodes.

Among many micro-structural parameters, the effect of mean particle diameter on the PEN performance was studied first for its importance. Reducing mean particle diameter by half results in four times larger TPB length in electrode, but it also reduces the Knudsen diffusivity to half and flow permeability to one fourth. In Figs. 7a and 8a, the dependence of PEN I - V perfor-

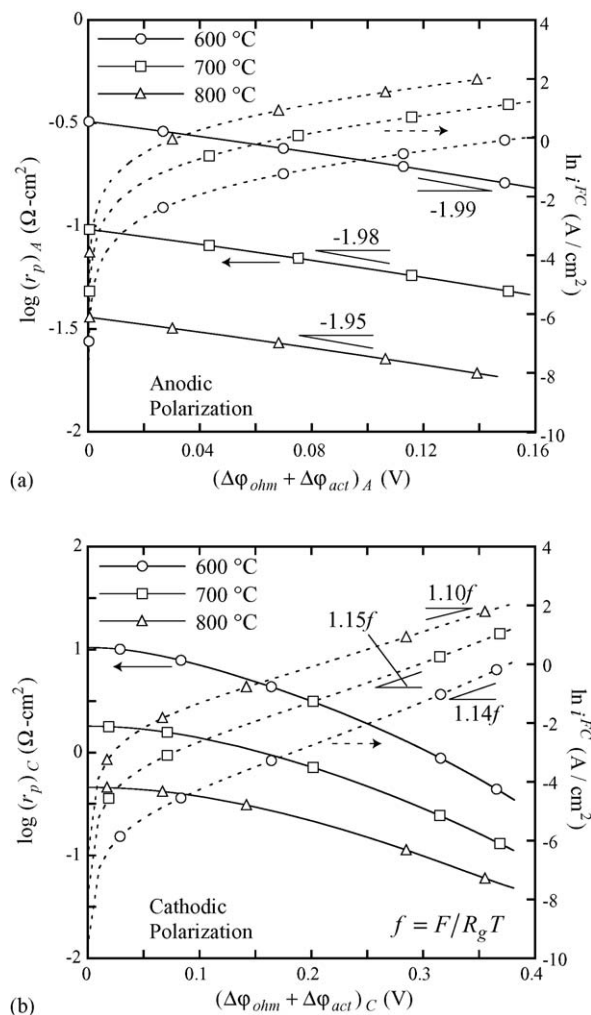


Fig. 6. Activation overpotential characteristic of anode (a), and that of cathode (b).

mance on the particle diameter in anode and that in cathode is shown. In general, smaller particle diameter results in better PEN performance, primarily due to increase in the density of TPBs or TPB length in the electrodes. However, the particle diameter in anode does not significantly enhance the PEN performance at low potential loss condition, as indicated by rather constant initial resistance in Fig. 7a, which is due to the relatively small contribution of anodic overpotential to overall potential loss at low potential loss conditions, observed in Fig. 4b. On the contrary, the particle size in cathode has significant effect on PEN I - V performance at all potential loss conditions for its contribution is always largest.

One may assume the existence of constant coefficients that include the effects of Darcy flow, binary diffusion and Knudsen diffusion in electrodes, e.g., an apparent diffusivity for hydrogen in anode $D_{H_2}^{app}$ or that for oxygen in cathode $D_{O_2}^{app}$. If we assume that all the electro-chemical reaction occurs near the electrode/electrolyte interface, $(p_{H_2})_{A/E}$ can be expressed as

$$(p_{H_2})_{A/E} = p_{H_2,\infty} - 10,000 \frac{i^{FC}}{2F} L_A R_g T \frac{1}{D_{H_2}^{app}}, \quad (41)$$

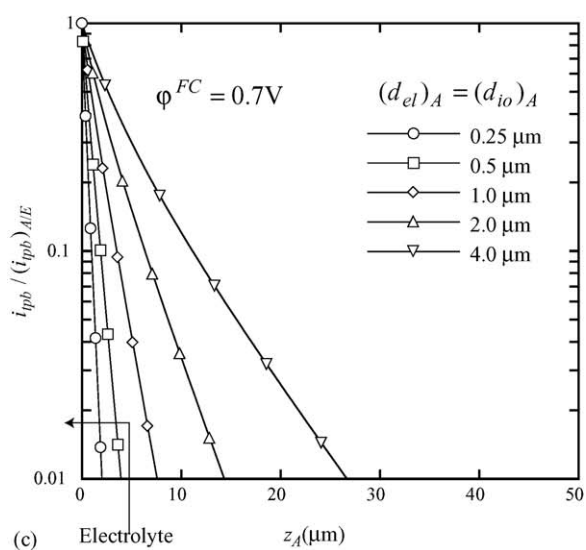
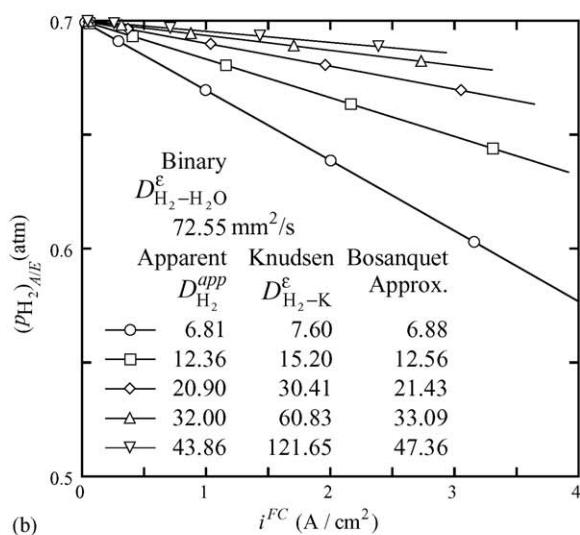
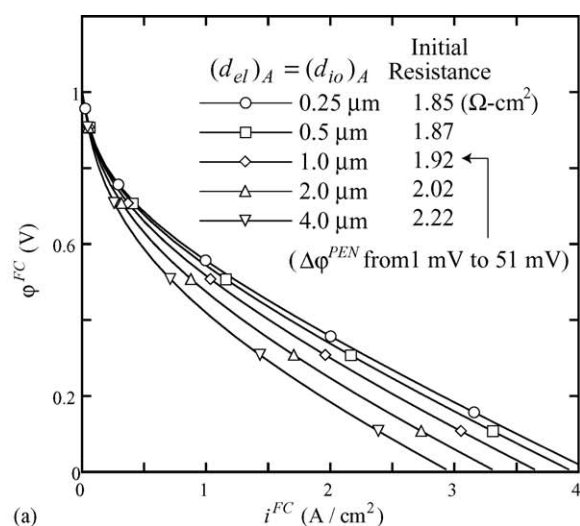


Fig. 7. Effect of anode particle size on PEN I - V performance (a), partial pressure of hydrogen at cathode/electrolyte interface (b), and spatial distribution of normalized i_{ipb} in anode (c).

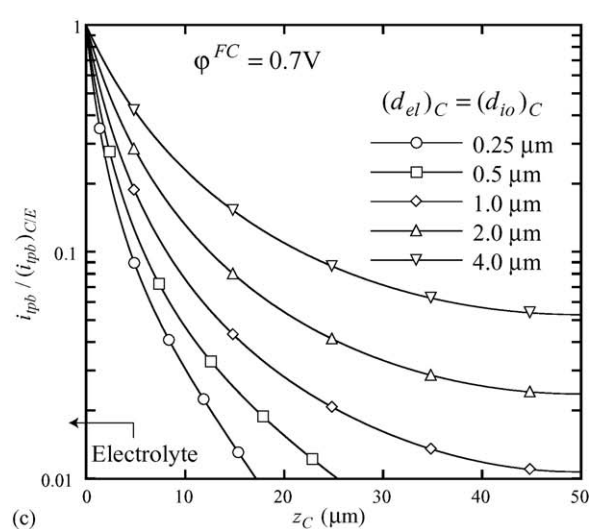
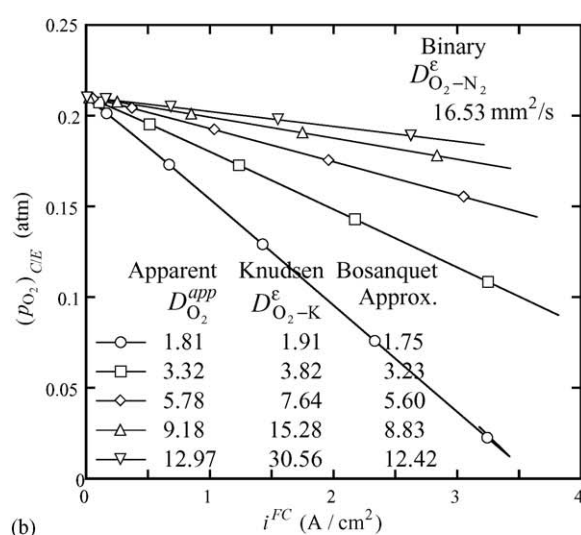
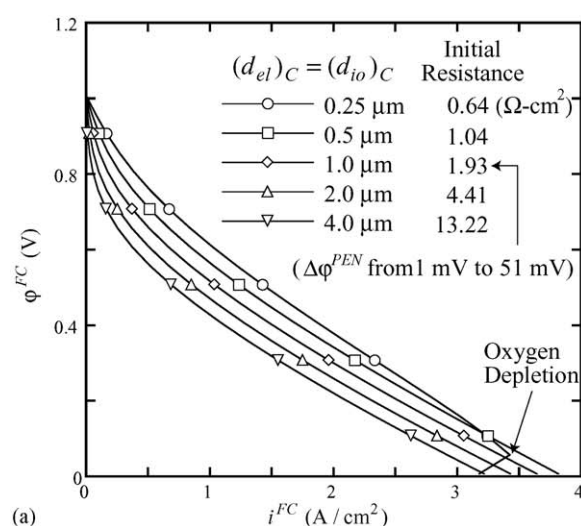


Fig. 8. Effect of cathode particle size on PEN I - V performance (a), partial pressure of oxygen at cathode/electrolyte interface (b), and spatial distribution of normalized i_{ipb} in cathode (c).

and, likewise, $(p_{O_2})_{C/E}$ can be expressed as

$$(p_{O_2})_{AC/E} = p_{O_2,\infty} - 10,000 \frac{i^{FC}}{4F} L_C R_g T \frac{1}{D_{O_2}^{app}}. \quad (42)$$

From the observed mean slopes of curves in Figs. 7b and 8b, the apparent diffusivities for hydrogen in anode and those for oxygen in cathode were obtained using Eqs. (41) and (42). The apparent diffusivities for hydrogen in Fig. 7b and those for oxygen in Fig. 8b are always smaller than their binary diffusivities $D_{H_2-H_2O}^e$ or $D_{O_2-N_2}^e$, primarily due to small Knudsen diffusivities in electrodes. Figs. 7b and 8b clearly shows that the dependence of apparent diffusivities on their particle diameters, for example, reduction of particle diameter from 1 to 0.5 μm results in decrease of the apparent diffusivity by about 40% for both electrodes.

Bosanquet approximation is generally used to obtain the effective diffusivity, by combining the effects of binary diffusion and Knudsen diffusion. The effective diffusivities for hydrogen in anode and oxygen in cathode are predicted by the Bosanquet approximation as

$$D_{H_2}^{eff} = \left(\frac{1}{D_{H_2-H_2O}^e} + \frac{1}{D_{H_2-K}^e} \right)^{-1}, \quad (43)$$

$$D_{O_2}^{eff} = \left(\frac{1 - x_{O_2,\infty}}{D_{O_2-N_2}^e} + \frac{1}{D_{O_2-K}^e} \right)^{-1}. \quad (44)$$

Figs. 7b and 8b indicate that the apparent diffusivities are relatively well estimated by the Bosanquet approximation; the differences are only about 1% for particle diameter of 0.25 μm , 2.4% for 1 μm , and 7.4% for 4 μm in anode, while they are about 3.4% for particle diameter of 0.25 μm , 3.2% for 1 μm , and 4.4% for 4 μm in cathode. Note that mole fraction of oxygen in cathode channel ($x_{O_2,\infty} = 0.21$) was used for Eq. (44), which may result in larger error in estimation of the effective diffusivity in cathode. In addition, the differences are also partially due to the assumption that all electro-chemical reaction occurs near the electrode/electrolyte interface. While such assumption may hold for anodic reaction, it does not for cathodic reaction as the cathodic reaction occurs in more extended region from the cathode/electrolyte interface. Further investigation showed that the Darcy flow effect was not very large in both electrodes; flow effect decreased $D_{H_2}^{app}$ by about 3% while it increased $D_{O_2}^{app}$ by about 1% for particle diameter of 1 μm .

The spatial distribution of i_{tpb} at Ni/YSZ TPBs in anode and that at LSM/YSZ TPBs in cathode, normalized by their maximums at the electrode/electrolyte interfaces, are presented in Figs. 7c and 8c. Smaller particle size provides larger TPB length in electrodes and thus results in lower activation losses, which is well observed in the figures. It is found again that most of electro-chemical reaction occurs within distance from electrolyte less than 10 μm for anode with 1 μm particle diameter. However, for cathode with 1 μm particle diameter, electro-chemical reaction seems to occur throughout the cathode thickness of 50 μm . Therefore, Figs. 7c and 8c can be a useful design guideline to determine the electrode thickness with different particle size.

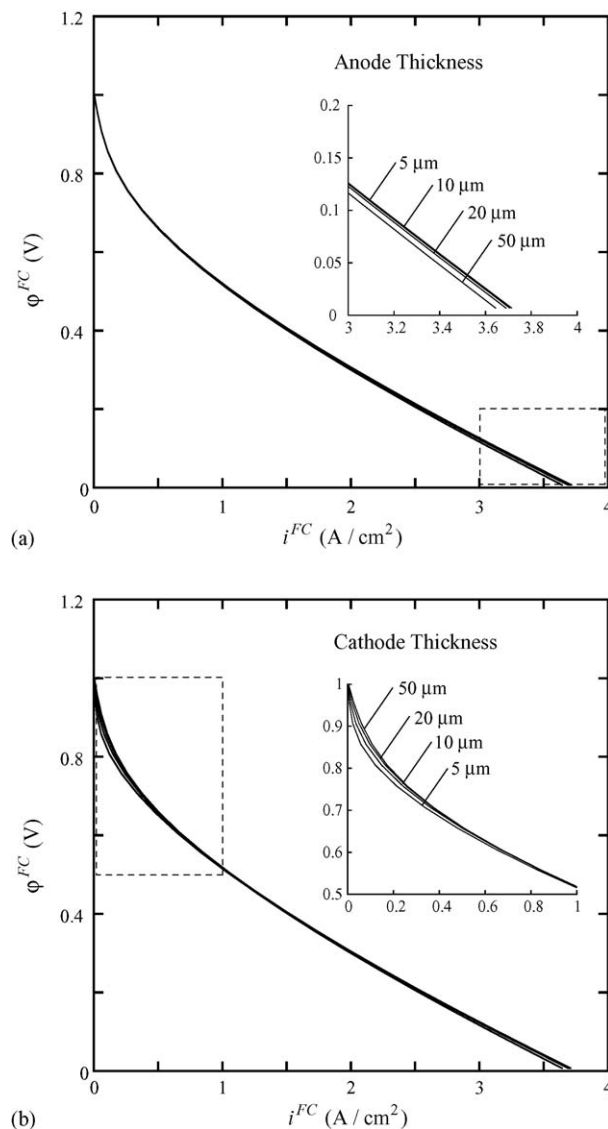


Fig. 9. Effect of electrode thickness on PEN I - V performance; anode thickness variation (a), and cathode thickness variation (b).

The PEN I - V performance curves in Fig. 9a exhibit no noticeable dependence on the anode thickness at low current density condition, which reconfirms that the anode thickness of 10 μm is sufficient as Fig. 7c demonstrated. Small performance difference at high current density condition is believed to be related with anodic concentration overpotential. Fig. 9b shows slight enhancement in PEN performance with larger cathode thickness at low current density condition, but it is not significant compared with the enhancement of PEN performance by reduction in mean particle size shown in Fig. 8a. Smaller mean particle size increases TPBs everywhere in electrodes (by increasing the density of TPBs) while thicker electrode increases TPBs whose distance from the electrolyte is largest (by adding TPBs).

The effect of cathode thickness on cell current density i^{FC} and area specific cathodic activation overpotential resistance $(r_p)_C$ is studied in Fig. 10. Smaller cathode thickness was required to

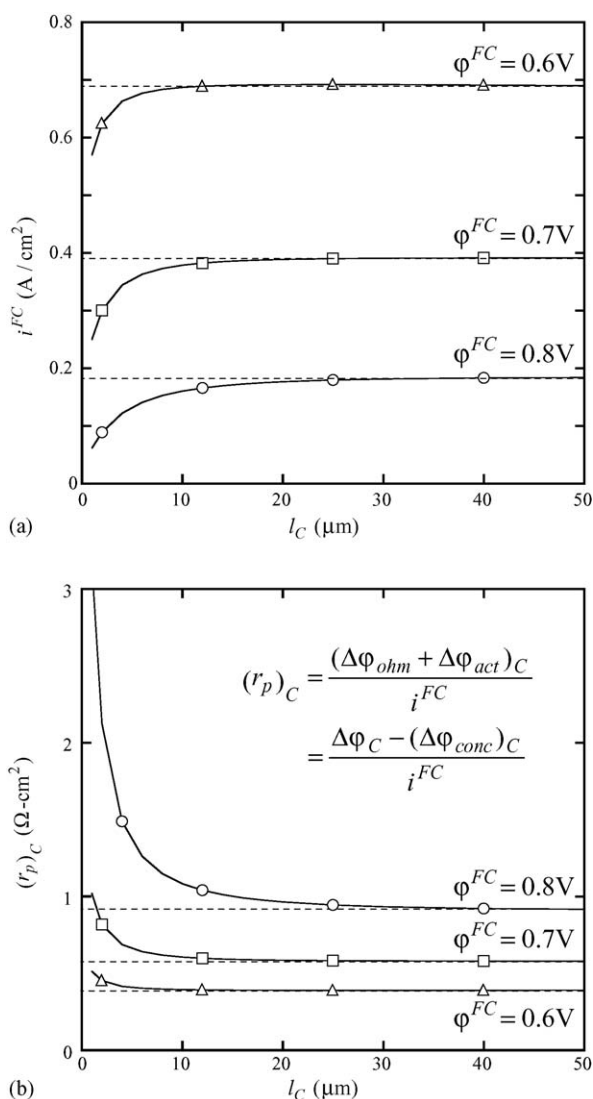


Fig. 10. Effect of cathode thickness variation on cell current density (a), and cathodic activation overpotential resistance (b).

obtain converged i^{FC} or converged $(r_p)_C$ when $\Delta\phi^{PEN}$ increased (or cell current density increased). As shown in Figs. 5a and 8c, the relative importance of TPBs near the electrolyte becomes more prominent as current density increases. This is also inferred from Fig. 9b, where the PEN I - V performance curves become identical at high current density before concentration activation overpotential starts to appear.

The composition of electronic and ionic phase in electrode has been extensively studied by many researchers, where the volume fraction of electronic phase ϕ_{el} of around 0.45 was found optimal. The optimal composition should provide percolation of both electronic and ionic phases, and also largest TPB length in electrodes. The PEN I - V performance curves for $\phi_{el} = 0.4$ and $\phi_{el} = 0.5$, shown in Fig. 11, are almost identical, representing best performance in $0.4 < \phi_{el} < 0.5$. The optimal composition was further investigated in Fig. 12, where the cell current density i^{FC} and activation overpotential resistance $(r_p)_A$ or $(r_p)_C$ at $\phi^{FC} = 0.7\text{V}$ are compared with varying ϕ_{el} from 0.3

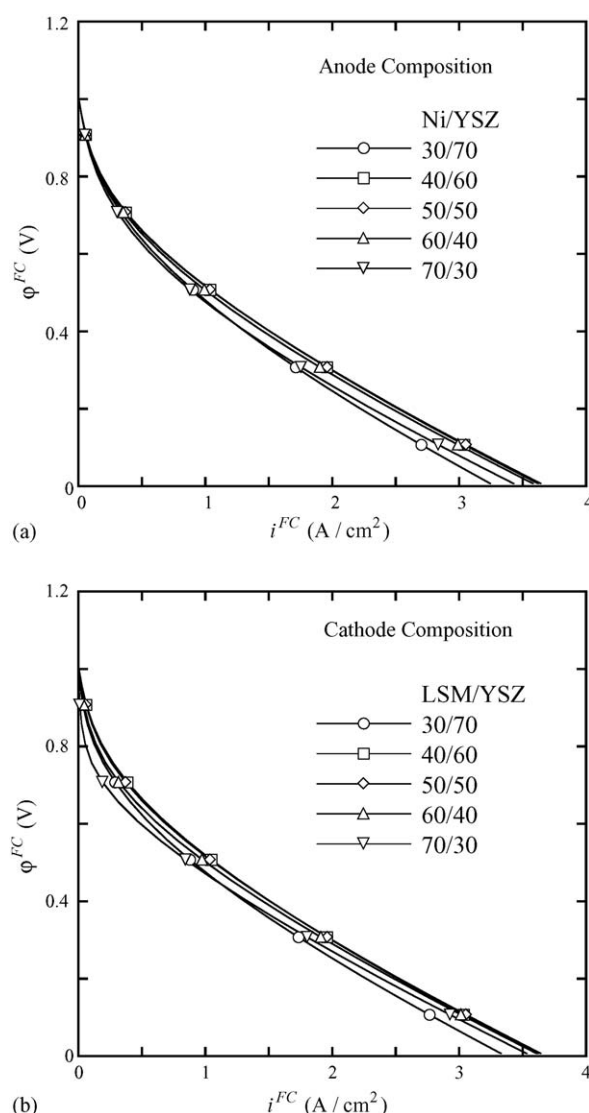


Fig. 11. Effect of electrode composition on PEN I - V performance; anode composition variation (a), and cathode composition variation (b).

to 0.7 (assuring percolation of both electronic and ionic phase). Fig. 12 shows that the performance reaches maximum at about 0.45 for both anode and cathode, which is well-matched with the theoretical and experimental observation by Costamagna et al. [13].

Finally, the effect of porosity is considered in Fig. 13, but in this case, more realistic geometry was considered by assuming anode thickness to be $500\text{ }\mu\text{m}$. Reducing electrode porosity leads to slight increase in solid volume fraction and thus TPB length in electrodes. However, at the same time, it decreases the mass transport rate by reducing Knudsen diffusivity, binary diffusivity and flow permeability. For example, reduction of porosity from 0.3 to 0.2 increase TPB length by about 12% (proportional to solid volume change from 0.7 to 0.8), but decreases the binary diffusivity by about 33% (proportional to pore volume change from 0.3 to 0.2 if tortuosity is constant), the Knudsen diffusivity by about 42%, and the flow permeability by about 77%.

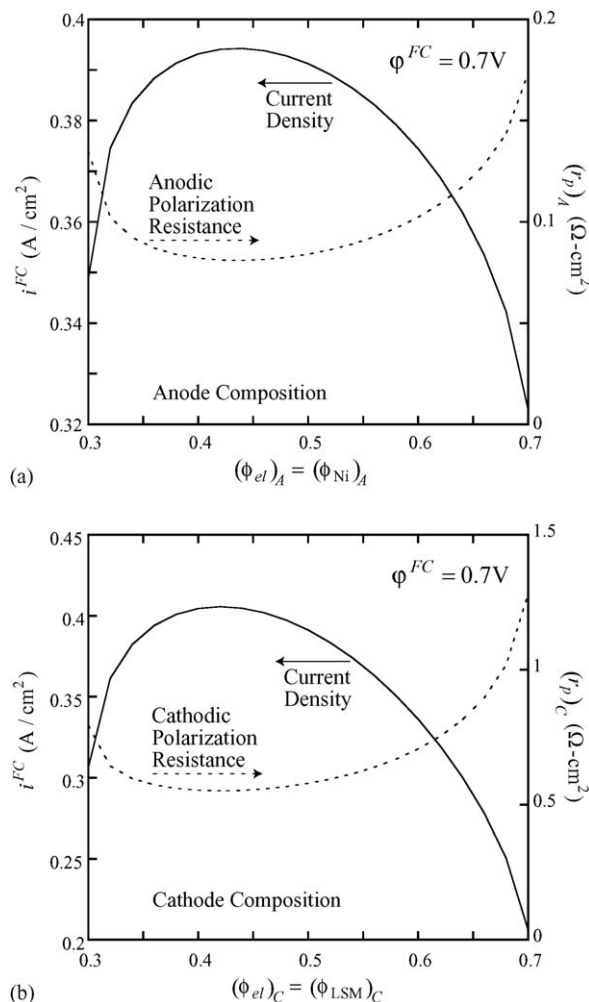


Fig. 12. Effect of electrode composition variation on cell current density and activation overpotential resistance; anode (a) and cathode (b).

Thus, to reducing the electrode porosity in order to increase larger TPB length is not desirable because of too large sacrifice in mass transport rate. It is better to reduce particle size to obtain larger TPB length; TPB length is inversely proportional to the square of particle size, while mass transport rate is roughly proportional to particle size (see Fig. 7b and c for apparent diffusivities).

Fig. 13a shows anode porosity of 0.3 results in concentration overpotential of about 0.05 V at the current density of 1.5 A/cm² (anode thickness of 500 μm). It is found that TPB length in anode is not generally limiting as shown by the PEN *I*-*V* performance. Therefore, increasing the anode porosity results in better performance by reducing the concentration loss at higher current density when mass transport becomes limiting. On the other hand, increasing the cathode porosity results in small difference in cathodic concentration overpotential for the small cathode thickness of 50 μm, and thus produces worse PEN performance with reduced TPB length. However, smaller cathode porosity does not always result in better SOFC performance, because the interconnect rib geometry for current collection increases mass transport resistance for oxygen significantly.

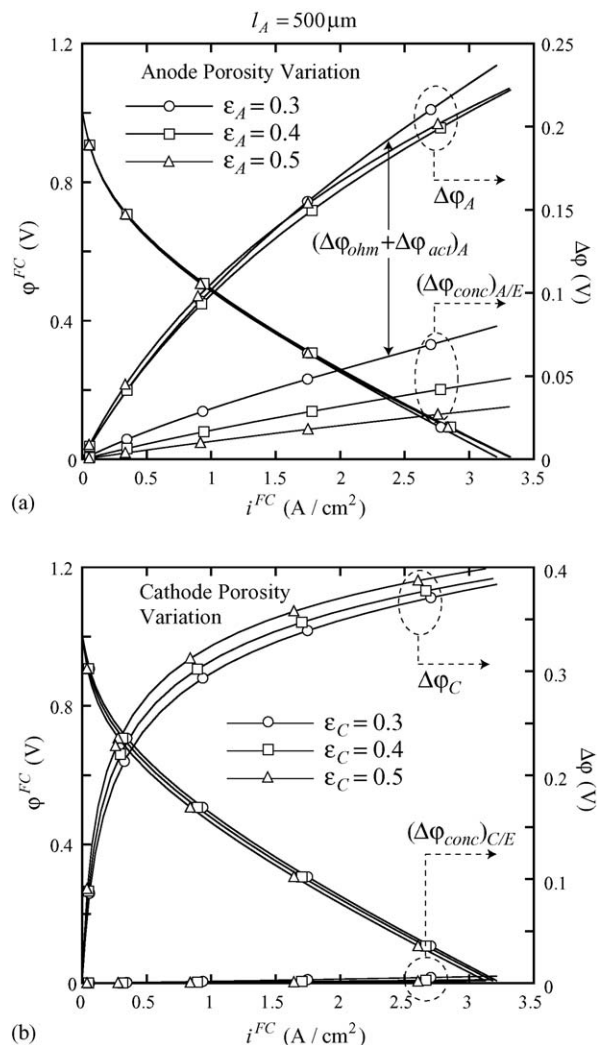


Fig. 13. Effect of electrode porosity on PEN *I*-*V* performance and overpotentials; anode porosity variation (a), and cathode porosity variation (b) (anode thickness is 500 μm).

5. Conclusion

In this study, a comprehensive micro-scale model for description of transport and reaction in SOFCs was developed, by combining many relevant theoretical and experimental studies of former researchers. Then, the developed micro-scale model and numerical procedure was used to characterize the dependence of PEN performance on several micro-structural parameters for both electrodes.

The potential loss in cathode was found most dominant at all current densities while the potential loss in anode was negligible at low current density but became important at higher current density. TPBs at the electrode/electrolyte interfaces were most active sites for electro-chemical reaction and its contribution increased at higher current density. The spatial gradient in total pressure was found to exist in both electrodes; that in cathode promoted the transport of oxygen while that in anode hindered the transport of hydrogen.

Among many micro-structural parameters for electrodes, the effect of particle size was found most prominent for the PEN

performance optimization. Smaller particle size reduced activation overpotential resistance by increasing TPB length in electrodes, but at the same time it increased the mass transport resistance by decreasing Knudsen diffusivity and flow permeability. Larger electrode thickness was found to produce better performance but the effect of electrode thickness was negligible at higher current density. The volume fraction of electronic phase of around 0.45 was found optimal for both anode and cathode, for the same ionic and electronic particle size. Higher porosity in anode and lower porosity in cathode resulted in better PEN performance for porosity higher than 0.3.

The porosity, particle size, and thickness of electrodes were found to have conflicting effects on the PEN performance. For example, reducing particle size in electrodes increased the efficiency of electro-chemical reaction but decreased the efficiency of mass transport. An optimal set of micro-structural parameters, which resulted in best PEN performance, will not automatically result in best SOFC performance. Micro-structural optimization of SOFC performance requires consideration on the interconnect rib geometry and the flow field effects, in addition to the detailed micro-scale calculation in PEN. The proposed micro-scale model is believed to be readily extended for such problems with more complex geometries, serving as a bridge between micro-scale models and macro-scale calculations.

Appendix A. Nomenclature

A_{ij}	common area of two finite volume i and j (m^2)
d	diameter of spherical particle (m)
d_c	neck diameter of TPB contacts (m)
d_h	hydraulic diameter for porous electrodes (m)
D_{ij}	binary diffusivity of gas pair i and j (m^2/s)
D_{iK}	Knudsen diffusivity of gas species i (m^2/s)
F	Faraday constant ($96,485 \text{ C mol}^{-1}$)
i	area specific current density (A m^{-2})
i_{tpb}	TPB length specific transfer current density (A/m)
I_{tpb}	transfer current in a finite volume, from ionic to electronic phase (A)
$I_{i \rightarrow j}$	electrical current from a finite volume i to j (A)
K	flow permeability (m^2)
Δl_{ij}	distance between two finite volumes i and j (m)
l_{tpb}^A	area specific TPB length at electrode/electrolyte interface (m/m^2)
l_{tpb}^V	volume specific TPB length (m/m^3)
L_{tpb}	TPB length contained in a finite volume (m)
M_i	molecular mass of gas species i (kg/mol)
$N_{k,i \rightarrow j}$	molar flow rate of gas species k , from a finite volume i to j (mol/s)
\dot{N}_k	molar generation of gas species k in a finite volume (mol/s^{-1})
p_i	partial pressure of gas species i (Pa)
p_t	total pressure (Pa)
P_i	percolation probability of i -phase
r_p	area specific activation resistance ($\Omega \text{ m}^2$)
r_{tpb}	TPB length specific charge transfer resistance ($\Omega \text{ m}$)

R_g	universal gas constant ($8.314 \text{ J K}^{-1} \text{ mol}^{-1}$)
R_{ij}	electrical resistance between two finite volumes i and j (Ω)
R_{tpb}	charge transfer resistance in a finite volume (Ω)
T	temperature (K or $^{\circ}\text{C}$)
ΔV_i	volume of a finite volume i (m^3)

Greek letters

ε	porosity of porous electrode
θ_c	neck angle of TPB contacts ($^{\circ}$)
μ	dynamic viscosity ($\text{kg m}^{-1} \text{ s}^{-1}$)
σ	electrical conductivity (S/m)
τ	tortuosity of porous electrode
ϕ_i	volume fraction of i -phase among solid volume
φ	electrical potential (V)
φ^0	Nernst potential (V)

Superscripts

FC	fuel cell operation condition
----	-------------------------------

Subscripts

act	activation loss
A	anode
conc	concentration loss
C	cathode
el	electronic
E	electrolyte
io	ionic
ohm	ohmic loss
∞	channel

References

- [1] N.Q. Minh, *J. Am. Ceram. Soc.* 76 (1993) 563.
- [2] J. Larminie, A. Dicks, *Fuel Cell Systems Explained*, Wiley & Sons, Chichester, 2000.
- [3] S. Sunde, *J. Electrochem. Soc.* 142 (1995) L50.
- [4] S. Sunde, *J. Electrochem. Soc.* 143 (1996) 1123.
- [5] S. Sunde, *J. Electrochem. Soc.* 143 (1996) 1930.
- [6] J. Abel, A.A. Kornyshev, W. Lehnert, *J. Electrochem. Soc.* 144 (1997) 4253.
- [7] D.H. Jeon, J.H. Nam, C.-J. Kim, *J. Power Sources* 139 (2005) 21.
- [8] M. Suzuki, T. Oshima, *Powder Technol.* 35 (1983) 159.
- [9] D. Bouvard, F.F. Lange, *Acta Metall. Mater.* 39 (1991) 3083.
- [10] C.-H. Kuo, P.K. Gupta, *Acta Metall. Mater.* 43 (1995) 397.
- [11] P. Costamagna, P. Costa, V. Antonucci, *Electrochim. Acta* 43 (1998) 375.
- [12] P. Costamagna, P. Costa, E. Arato, *Electrochim. Acta* 43 (1998) 967.
- [13] P. Costamagna, M. Panizza, G. Cerisola, A. Barbucci, *Electrochim. Acta* 47 (2002) 1079.
- [14] S.H. Chan, Z.T. Xia, *J. Electrochem. Soc.* 148 (2001) A388.
- [15] X.J. Chen, S.H. Chan, K.A. Khor, *Electrochim. Acta* 49 (2004) 1851.
- [16] S.H. Chan, X.J. Chen, K.A. Khor, *J. Electrochem. Soc.* 151 (2004) A164.
- [17] J. Mizusaki, H. Tagawa, T. Saito, T. Yamamura, K. Kamitani, K. Hirano, S. Ehara, T. Takagi, T. Hikita, M. Ippommatsu, S. Nakagawa, K. Hashimoto, *Solid State Ionics* 70–71 (1994) 52.
- [18] F.P.F. van Berkel, F.H. van Heuveln, J.P.P. Huijsmans, *Solid State Ionics* 72 (1994) 240.
- [19] S.P. Jiang, Y. Ramprakash, *Solid State Ionics* 116 (1999) 145.
- [20] S.P. Jiang, Y. Ramprakash, *Solid State Ionics* 122 (1999) 211.

- [21] B. de Boer, M. Gonzalez, H.J.M. Bouwmeester, H. Verweij, *Solid State Ionics* 127 (2000) 269.
- [22] A. Bieberle, L.J. Gauckler, *Solid State Ionics* 135 (2000) 337.
- [23] A. Bieberle, L.P. Meier, L.J. Gauckler, *J. Electrochem. Soc.* 148 (2001) A646.
- [24] F.H. van Heuveln, H.J.M. Bouwmeester, F.P.F. van Berkel, *J. Electrochem. Soc.* 144 (1997) 126.
- [25] F.H. van Heuveln, H.J.M. Bouwmeester, *J. Electrochem. Soc.* 144 (1997) 134.
- [26] E.P. Murray, T. Tsai, S.A. Barnett, *Solid State Ionics* 110 (1998) 235.
- [27] T. Horita, K. Yamaji, N. Sakai, Y. Xiong, T. Kato, H. Yokokawa, T. Kawada, *J. Power Sources* 106 (2002) 224.
- [28] J.-D. Kim, G.-D. Kim, J.-W. Moon, Y.-I. Park, W.-H. Lee, K. Kobayashi, M. Nagai, C.-E. Kim, *Solid State Ionics* 143 (2001) 379.
- [29] R. Radhakrishnan, A.V. Virkar, S.C. Singhal, *J. Electrochem. Soc.* (2005) A210.
- [30] E.A. Mason, A.P. Malinauskas, *Gas Transport in Porous Media: The Dusty Gas Model*, Elsevier, New York, 1983.
- [31] E.A. Mason, H.K. Lonsdale, *J. Membrane Sci.* 51 (1990) 1.
- [32] R. Krishna, J.A. Wesselingh, *Chem. Eng. Sci.* 52 (1997) 861.
- [33] J.R. Ferguson, J.M. Fiard, R. Herbin, *J. Power Sources* 58 (1996) 109.
- [34] U. Anselmi-Tamburini, G. Chiodelli, M. Arimondi, F. Maglia, G. Spinolo, Z.A. Munir, *Solid State Ionics* 110 (1998) 35.
- [35] W. Kiatkittipong, T. Tagawa, S. Goto, S. Assabumrungrat, P. Prasertthad, *Chem. Eng. J.* 106 (2005) 35.
- [36] J.-H. Lee, H. Moon, H.-W. Lee, J. Kim, J.-D. Kim, K.-H. Yoon, *Solid State Ionics* 148 (2002) 15.
- [37] H. Zhu, R.J. Kee, *J. Power Sources* 117 (2003) 61.
- [38] R. Suwanwarangkul, E. Croiset, M.W. Fowler, P.L. Douglas, E. Entchev, M.A. Douglas, *J. Power Sources* 122 (2003) 9.
- [39] E. Hernández-Pacheco, D. Singh, P.N. Hutton, N. Patel, M.D. Mann, *J. Power Sources* 138 (2004) 174.
- [40] M. Kaviany, *Principles of Heat Transfer in Porous Media*, 2nd ed., Springer, New York, 1999.
- [41] R.B. Bird, W.E. Stewart, E.N. Lightfoot, *Transport Phenomena*, 2nd ed., Wiley & Sons, New York, 2002.
- [42] B. Todd, J.B. Young, *J. Power Sources* 110 (2002) 186.
- [43] E.N. Fuller, P.D. Schettler, J.C. Giddings, *Ind. Eng. Chem.* 58 (1966) 19.
- [44] R.E. Williford, L.A. Chick, G.D. Maupin, S.P. Simner, J.W. Stevenson, *J. Electrochem. Soc.* 150 (2003) A1067.
- [45] F. Zhao, A.V. Virkar, *J. Power Sources* 141 (2005) 79.